



HAL
open science

Spatial Distribution of Electrochemical Performance in a Segmented SOFC: A Combined Modeling and Experimental Study

Wolfgang G Bessler, Stefan Gewies, Caroline Willich, Günter Schiller,
Andreas K Friedrich

► To cite this version:

Wolfgang G Bessler, Stefan Gewies, Caroline Willich, Günter Schiller, Andreas K Friedrich. Spatial Distribution of Electrochemical Performance in a Segmented SOFC: A Combined Modeling and Experimental Study. *Fuel Cells*, 2010, 10 (3), pp.411. 10.1002/fuce.200900083 . hal-00552354

HAL Id: hal-00552354

<https://hal.science/hal-00552354>

Submitted on 6 Jan 2011

HAL is a multi-disciplinary open access archive for the deposit and dissemination of scientific research documents, whether they are published or not. The documents may come from teaching and research institutions in France or abroad, or from public or private research centers.

L'archive ouverte pluridisciplinaire **HAL**, est destinée au dépôt et à la diffusion de documents scientifiques de niveau recherche, publiés ou non, émanant des établissements d'enseignement et de recherche français ou étrangers, des laboratoires publics ou privés.



Spatial Distribution of Electrochemical Performance in a Segmented SOFC: A Combined Modeling and Experimental Study

Journal:	<i>Fuel Cells</i>
Manuscript ID:	fuce.200900083.R2
Wiley - Manuscript type:	Original Research Paper
Date Submitted by the Author:	08-Dec-2009
Complete List of Authors:	Bessler, Wolfgang; German Aerospace Center, Institute of Technical Thermodynamics Gewies, Stefan; German Aerospace Center, Institut für Kommunikation und Navigation Willich, Caroline; German Aerospace Center, Institute of Technical Thermodynamics Schiller, Günter; German Aerospace Center, Institute of Technical Thermodynamics Friedrich, Andreas; German Aerospace Center, Institute of Technical Thermodynamics
Keywords:	Solid Oxide Fuel Cell, Segmented Cell, Experiment, Modelling, Simulation



Spatial Distribution of Electrochemical Performance in a Segmented SOFC: A Combined Modeling and Experimental Study

Wolfgang G. Bessler^{1,2*}, Stefan Gewies³, Caroline Willich¹, Günter Schiller¹, K. Andreas Friedrich¹

¹ Deutsches Zentrum für Luft- und Raumfahrt (DLR)
Institut für Technische Thermodynamik
Pfaffenwaldring 38-40
D-70569 Stuttgart / Germany

² Universität Stuttgart
Institut für Thermodynamik und Wärmetechnik
Pfaffenwaldring 6
D-70550 Stuttgart / Germany

³ Deutsches Zentrum für Luft- und Raumfahrt (DLR)
Institut für Kommunikation und Navigation
Kalkhorstweg 53
D-17235 Neustrelitz / Germany

* Corresponding author, email: wolfgang.bessler@dlr.de, phone: +49 711 6862603

Abstract

Spatially inhomogeneous distribution of current density and temperature in solid oxide fuel cells (SOFC) contributes to accelerated electrode degradation, thermomechanical stresses, and reduced efficiency. This paper presents a combined experimental and modeling study of the distributed electrochemical performance of a planar SOFC. Experimental data were obtained using a segmented cell setup that allows the measurement of local current-voltage characteristics, gas composition and temperature in 4×4 segments. Simulations were performed using a two-dimensional elementary kinetic model that represents the experimental setup in a detailed way. Excellent agreement between model and experiment was obtained for both global and local performance over all investigated operating conditions under varying H₂/H₂O/N₂ compositions at the anode, O₂/N₂ compositions at the cathode, temperature, and fuel utilization. A strong variation of the electrochemical performance along the flow path was observed when the cell was operated at high fuel utilization. The simulations predict a considerable gradient of gas-phase concentrations along the fuel channel and through the thickness of the porous anode, while the gradients are lower at the cathode side. The anode dominates polarization losses. The cell may operate locally in critical operating conditions (low H₂/H₂O ratios, low local segment voltage) without notably affecting globally observed electrochemical behavior.

Keywords: Solid oxide fuel cell (SOFC), Segmented cell, Experiment, Modeling, Simulation

1 Introduction

High electrical efficiency and long-term durability are key requirements for a cost-competitive introduction of fuel cell technology. In order to achieve high efficiency, a high fuel utilization is required, that is, the complete fuel should be converted electrochemically in the fuel cell. In solid oxide fuel cells (SOFC), high fuel utilization results in strong concentration gradients at the anode, where the fuel (H₂, CO, CH₄) is successively diluted by reaction products (H₂O, CO₂). This, in turn, leads to an inhomogeneous distribution of electrochemical performance (local power density) and temperature. These inhomogeneities detrimentally affect both efficiency (through a large concentration polarization) and long-term stability (through thermomechanical stresses and local operating conditions that may induce degradation). In order to understand these effects, it is necessary to obtain detailed information about the spatial distribution of the electrical, chemical and thermal cell properties.

For polymer electrolyte fuel cells (PEFCs), segmented cell setups for the local measurement of current density have been developed and are widely used¹⁻⁷. In contrast to this, only few experiments for a spatially resolved characterization of SOFCs have been conducted so far, mainly because the high operating temperature (700-900 °C) represents a considerable challenge to the experimental setup. One of the first setups for the local characterization of segmented planar SOFC cells has been developed by Metzger et al.⁸⁻¹⁰.

Segmented-cell setups are typical model experiments in the sense that they allow a largely extended insight at the cost of modified geometries and/or materials in comparison to standard fuel cells. Results from segmented cells are therefore not expected to be quantitatively equivalent to those from standard stacks in terms of performance or temperature distribution. Having this difference in mind, the accessible information is highly valuable both for increasing the fundamental understanding and for optimizing cell and flow field design.

The use of mathematical modeling in combination with experimental investigations can significantly enhance the understanding of the spatially resolved electrochemical behavior of the cell. For example, today's experimental techniques do not allow the measurement of concentration and current distributions inside the porous electrodes. However, it is the electrochemically active zone inside the electrodes that governs electrochemical performance as well as degradation behavior. For this reason, modeling studies are increasingly used to aid understanding of the fuel cell processes and to optimize electrode and cell design^{11,12}. The combination of simulations with segmented-cell experiments is particularly useful because it allows reliable model validation including local behavior. Furthermore, the segmentation can easily be omitted and geometrical parameters be modified in the model, thus allowing to bridge the difference between the segmented cells and standard cells.

In this paper we present a combined modeling and experimental study of the spatial distribution of electrochemical performance in a planar SOFC. The experiments are based on the setup by Metzger et al.⁹. The simulations are conducted within a physically-based modeling framework developed by Bessler et al.¹³, which is extended in order to reflect the segmentation of the experimental setup. The following approach is used: (i) The model is validated using experimental polarization data under specifically designed calibration conditions; (ii) model predictions are compared with experimental data at realistic operating conditions; and (iii) the validated model is used for quantitative interpretation and prediction of the physical, electrochemical and fluid mechanical fuel cell properties.

2 Experimental Setup

The measurement setup for segmented cells has been described previously^{8,9}. It is shown schematically in Fig. 1a. Square-shaped anode-supported cells (100 cm² area, 540 μm Ni/YSZ cermet anode with a thin anode functional layer, 5 μm 8YSZ electrolyte, 3 μm YDC interlayer, 45 μm LSCF cathode divided into 16 segments with an active area of 4.84 cm² of each segment) were integrated in a metallic cell housing and sealed with glass seal (Fraunhofer Institute of Ceramic Technologies and Sintered Materials (IKTS), Dresden, Germany). The metallic housing is subdivided into 16 galvanically isolated segments with a total active area of 73.96 cm². The flow field is identical for fuel and air side; it consists of square-shaped channels (2 × 2 mm, 5 channels per segment row) that are supplied via inlet and outlet manifolds that are symmetrical to each other (ca. 4 cm³ per manifold).

In order to determine the temperature at each segment, thermocouples are introduced in the metallic segments. Additionally, capillary tubes that correspond to the cathodic segments are integrated at the anode side at 16 measuring points to take samples of the anode gas to be analyzed by gas chromatography. The setup allows for the integral and spatially resolved measurement of current density and voltage, the local and integral determination of impedance data, the local measurement of temperature and the spatially resolved analysis of the fuel gas concentrations along the flow path.

Experiments were conducted under a wide range of operating conditions as summarized in Table 1. Conditions for model calibration were defined that show a high sensitivity of simulated polarization curves on unknown model parameters. The calibration measurements were carried out under high gas flow rates (low fuel utilization) in order to avoid strong fuel depletion. Even for the highest fuel dilution (Table 1, condition 6), fuel utilization was < 26 %. Additional measurements were performed under realistic gas compositions at high fuel utilization (Table 1, condition 10).

3 Modeling and Simulation

3.1 Planar SOFC Modeling Framework

The framework for physically-based SOFC modeling and simulation has been presented previously¹³. The model layout is shown schematically in Fig. 2, and all model parameters are summarized in Table 2. A detailed 1D+1D elementary kinetic electrochemical model was applied that represents one single channel of the experimental setup (Fig. 2b). One-dimensional channel flow (*x* dimension) is described using the Navier-Stokes conservation equations (continuity, species, momentum), corresponding essentially to a plug-flow model with axial diffusion¹⁴. One-dimensional mass transport through the membrane-electrode assembly (MEA) (*y* dimension) is described by coupled Fickian/Knudsen diffusion and Darcy flow. Charge transport in the solid

electrolyte and the electrolyte phase of the composite electrodes is described in two dimensions using Ohm's law.

The results shown in this paper are calculated under the assumption of isothermal conditions. This assumption is justified because measured temperature variations along the flow path are relatively low (26 K at a current density of 1.4 A/cm²) due to rapid heat losses via the metallic flow field and housing.

Anode electrochemistry is described using elementary kinetics for surface reactions on Ni and YSZ, and for charge transfer (hydrogen spillover) (Fig. 2c), as given in Table 3, and as validated by previous cermet anode and patterned anode studies^{15, 16}. The electrochemical double layer is described as simple capacitor. Cathode electrochemistry is described using a modified Butler-Volmer equation,

$$i = i^0 p_{O_2}^a \exp(-E_{act} / RT) \cdot [\exp(0.5F\eta/RT) - \exp(-0.5F\eta/RT)] . \quad (1)$$

A definition of all symbols and their units is given in¹³. Current-voltage relationships are modeled by directly solving for the electric-potential distribution in the electrodes and electrolytes without using the Nernst equation. All models are implemented in the in-house numerical simulation software DENIS. For numerical simulation, the MEA was spatially discretized into 16 × 80 control volumes (x × y dimension). For identifying unknown model parameters, a Levenberg-Marquardt nonlinear least-squares fitting algorithm was used¹⁷.

3.2 Segmentation

For the present study, the model described in Ref.¹³ was extended in order to include the cell segmentation of the experimental setup. The segmentation is represented by an electrical circuit model as shown in Fig. 2a. An arbitrary number and size of segments can be used at both anode and cathode. The segments are individually connected via switches S_i to outer power rails at anode and cathode side. These rails are assumed to be at constant potential ϕ given by the outer load. The connection wires are assumed to be resistors R_i , leading to a potential drop modeled via Ohm's law,

$$\Delta\phi = R i_{seg} , \quad (2)$$

where R is the cell-area-specific wire resistance and the potential drop $\Delta\phi$ depends on the segment current density i_{seg} . Along the length of each individual segment the potential and therefore the local segment voltage U_{local} are assumed constant. The simulation input is the voltage U of the external load. The model yields the total current I , the individual segment currents I_i , as well as local segment voltages U_{local} . The latter are determined experimentally via individual voltage probes (four-point measurements at each segment). The model can also be used to calculate global and local impedance Z and Z_{local} , respectively.

For the present simulations, four segments are used at both anode and cathode, and all switches S_i are closed, representing the experimental setup. The wire resistance R is determined via fitting to the experiments (cf. Table 2).

4 Results and Discussion

4.1 Calibration Measurements and Model Validation

There are a number of model parameters associated with electrochemistry and transport in the MEA that are specific for the investigated cells and cannot be obtained from literature. Some parameters can be reliably estimated (e.g., porosity from SEM micrographs). Other parameters, however, can only be obtained by fitting to experimental data. To this goal, the model was validated under specifically designed operating conditions (Table 1, conditions 1-9). Experimental polarization behavior was measured under low fuel utilization (< 15 % by using fast gas inflow velocities) in order to circumvent spatial gradients along the channel. Gas-phase anode and cathode inlet concentrations as well as temperature were varied over a range of conditions; these conditions were chosen in order to achieve sensitivity for the unknown parameters. Parameters were fitted using a one-dimensional model of the MEA only. Fitting results are included in Table 2 and Table 3.

In the present study, the following model parameters were fitted: (1) The preexponential factor of the elementary kinetic hydrogen spillover reaction at the anode (all other elementary kinetic parameters were used without modification from previous cermet anode studies¹⁵); (2) the exchange current density of the global kinetic charge-transfer reaction at the cathode; (3) the p_{O_2} exponent for cathode; (4) the tortuosity of the anode; (5) the ohmic resistance of the current collector wires. Given the high level of physicochemical detail of the present model, the number of free fit parameter has to be considered very low. It should be noted that the preexponential factor of the anodic charge-transfer reaction had to be modified by only 30 % in comparison to previous cermet anode studies¹⁵; this small modification can be interpreted as variations in material and/or microstructure and demonstrates how elementary kinetic approaches can reduce empiricism in fuel cell modeling.

1
2
3 Simulated and experimental polarization curves for the validation conditions are shown in Fig. 3. There is
4 good quantitative agreement between model and experiment over the complete range of operating conditions
5 (anode H_2/H_2O ratio, anode gas dilution with N_2 , cathode O_2/N_2 ratio, and temperature). Note that the physical
6 model uses only one single set of parameters for all conditions. A systematic deviation between model and
7 experiment occurs during temperature variation. We believe that this is due to an onset of cell degradation,
8 lowering the experimentally observed performance relative to the model predictions. Degradation effects are not
9 included in the model.

11 4.2 Measurement and Simulation Under High Fuel Utilization

12 The segmented cell was operated under a condition with high fuel utilization (Table 1, condition 10). The
13 anode was fed with 33% H_2 , 1% H_2O and 66% N_2 . This condition was chosen in order to simulate nitrogen-rich
14 reformate gas. The cathode was fed with air in counter-flow operation.

15 The measured two-dimensional distribution of power density in the 16 segments is shown in Fig. 4 for an
16 average power density of 460 mW/cm^2 . The fuel utilization at this condition is 80%. The cell performance is
17 strongly inhomogeneous, with the power density systematically decreasing from fuel inlet (left side of Fig. 4) to
18 fuel outlet (right side of Fig. 4). It will be shown below that this decrease is due to fuel depletion along the flow
19 path. Moreover, there is a notable difference for the four segment rows (upper row to lower row in Fig. 4). This
20 difference may be due to sealing issues or inhomogeneous gas supply to the gas channels. Further segment-to-
21 segment scattering is likely due to a variation in contact resistance, which may also lead to systematic row-to-
22 row variations when the contact pressure is inhomogeneous. For comparison with the model (which represents
23 the behavior along one single channel), the row with segments 9-12 was chosen.

24 Experimental and simulated global and local current-voltage characteristics for segments 9-12 are shown in
25 Fig. 5. Simulations were performed using the 2D model (i.e., along one representative channel and through the
26 thickness of the MEA, cf. Fig. 2). The global IV-curve (Fig. 5a) shows a typical shape with a parabolic behavior
27 at low currents, linear behavior at intermediate currents, and a limiting current density of $\sim 0.8 \text{ A/cm}^2$ at high
28 currents. The maximum power density ($P_{\max} = 470 \text{ mW/cm}^2$) is observed at a cell voltage of 0.70 V. Local IV-
29 curves for segments 9-12 are represented by plotting local segment voltage versus local segment current (Fig.
30 5b). The local behavior shows a considerable variation of current density for different cell segments. At high
31 polarization, segments 11 and 12 that are located close to the fuel outlet show a particularly interesting behavior:
32 the current decreases while at the same time the segment voltage strongly decreases. This "inverse" behavior is
33 due to strong fuel depletion (see next section). At the same time, the current density of segment 9 that is located
34 at the fuel inlet continues to increase.

35 There is excellent quantitative agreement between model and experiment for both the local and the global
36 behavior. Note that no additional parameter adjustment was performed after model calibration (Section 4.1). This
37 finding also underlines the validity of the choice of calibration conditions.

39 4.3 Distribution of Gas-Phase Concentrations

40 Fig. 6 shows the simulated spatially resolved distribution of gas-phase concentrations in the channels as well
41 as in the porous electrodes and current collector meshes for the condition of maximum power density (P_{\max} in
42 Fig. 5a). There are considerable concentration gradients throughout the complete system. In particular, the
43 relatively thick porous anode in this anode-supported cell is responsible for strong H_2 depletion through the
44 anode thickness. This is the case, in particular, for segments 11 and 12. Here, H_2 concentration tends towards
45 zero at the porous electrode/solid electrolyte interface. This is the reason for the strong decrease in segment
46 voltage observed in the local IV-curves (Fig. 5b).

47 The upper panel of Fig. 6 also shows the local current density along the flow path. The step-like behavior of
48 the four segments is due to the contribution of the resistance of current collector wires (cf. Fig. 2a): The potential
49 drop over the wire for the individual segments decreases as the overall segment current decreases along the fuel
50 flow path (left to right in Fig. 6). This leads to an increase in integral segment current, causing a step from the
51 end of one segment to the beginning of the next segment. Note that the segment voltage is measured and
52 simulated directly at the segment (U_{local} in Fig. 2a), therefore including the wire resistance. The current density
53 distribution along the length of each segment is inhomogeneous. The integral current density over one segment is
54 shown in Fig. 5b.

55 The condition of strong fuel depletion observed inside the porous anode may be highly critical concerning
56 cell degradation. In particular, low H_2/H_2O ratios may lead to nickel oxidation at the anode, and low local
57 segment voltages may lead to cathode degradation¹⁸. Note that the critical behavior observed here in particular
58 at segment 12 is not obvious from the global IV-behavior. Thus, a cell may be locally in a critical operating
59 condition while global characteristics are well within apparent stability limits (e.g., sufficiently high global cell
60 voltage). Post-test analysis and interpretation with a focus on degradation is subject of ongoing studies.

4.4 Distribution of Polarization Losses

The knowledge of the physical origin of polarization losses is a requirement for an optimization of cell design and operating conditions. The validated model offers the possibility to quantify the spatially varying polarization losses. Results for segments 9 and 12 are shown in Fig. 7 for the same operating conditions as shown in Fig. 5. The total polarization losses are separated into contributions from Ohmic resistance of the electrolyte η_{ohm} , concentration polarization η_{conc} at both anode and cathode, and activation polarization η_{act} at both anode and cathode.

For both segments, concentration polarization at the anode is the dominant loss process. This finding is consistent with the observation of strong H_2 depletion along the channel and through the anode thickness. The second largest contribution is anode activation. Polarization due to the electrolyte and cathode activation and concentration losses are low and do not significantly affect the cell performance. With increasing current density, all losses increase up to the point of maximum power density. Beyond that point, Ohmic and activation losses decrease in segment 12 due to the decreasing local current density in these segments (cf. Fig. 5b).

The analysis shows that the parabolic behavior at low current density that is observed in the global IV-curve (Fig. 5a) is due to anode concentration polarization and not, as commonly assumed, due to activation polarization. This has been pointed out before¹⁴. In this respect, SOFCs behave differently from PEFCs where low-current parabolic behavior is indeed due to activation losses.

5 Conclusions

A combined experimental and modeling study of the spatial distribution of the electrochemical performance in a planar SOFC was performed. Experimental data were obtained using a specifically designed segmented cell setup that allows for the measurement of local current-voltage characteristics, gas composition and temperature. Simulations were performed using a two-dimensional elementary kinetic model that represents the experimental setup in a highly detailed way.

Model parameters were identified by comparing simulations with validation experiments under low fuel utilization. Experiments and simulations under high fuel utilization showed strong gradients of gas concentrations and current density along the flow path and throughout the thickness of the membrane-electrode assembly. Over the complete range of operating conditions, excellent quantitative agreement between model and experiment for both global and local behavior was observed. The relatively thick porous anode and high fuel utilization causes particularly strong concentration variations at the anode, while the gradients are lower at the cathode side. The combined modeling and experimental study allows for the reliable quantification of the contribution of various polarization losses. It was shown that concentration polarization at the anode is the dominant loss process, followed by anode activation polarization. The anode was therefore identified as the critical component in this cell type.

An important conclusion is that the cell may operate locally in critical operating conditions (low $\text{H}_2/\text{H}_2\text{O}$ ratios, low local segment voltage) without notably affecting global electrochemical behavior. These conditions are likely to detrimentally affect cell durability. Based on a combination of experiment and modeling, the present study allows for identifying such conditions and for assessing optimized cell design and operation strategies.

Acknowledgements

Funding was provided by the Umweltministerium Baden-Württemberg, Germany, through the programme "Herausforderung Brennstoffzelle" (ZO4 BW26037 and ZO4 BW26038).

References

1. M. Noponen, T. Tennola, M. Mikkola, T. Hottinen and P. Lund, *J. Power Sources*, 2002, **106**, 304-312.
2. D. J. L. Brett, S. Atkins, N. P. Brandon, V. Vesovic, N. Vasileiadis and A. R. Kucernak, *Electrochemistry Communications*, 2001, **3**, 628-632.
3. N. Rajalakshmi, M. Raja and K. S. Dhathathreyan, *J. Power Sources*, 2002, **112**, 331-336.
4. G. Bender, M. S. Wilson and T. A. Zawodzinski, *J. Power Sources*, 2003, **123**, 163-171.
5. S. Schönbauer and H. Sander, in *3rd European PEFC Forum*, Lucerne, Switzerland, 2005, p. B056.
6. I. A. Schneider, S. A. Freunberger, D. Kramer, A. Wokaun and G. G. Scherer, *J. Electrochem. Soc.*, 2007, **154**, B383-B388.
7. M. Schulze, E. Gülzow, S. Schönbauer, T. Knöri and R. Reissner, *J. Power Sources*, 2007, **173**, 19-27.
8. P. Metzger, G. Schiller and A. O. Störmer, in *6th European Solid Oxide Fuel Cell Forum*, Lucerne, Switzerland, 2004, pp. 989-999.
9. P. Metzger, K.-A. Friedrich, H. Müller-Steinhagen and G. Schiller, *Solid State Ionics*, 2006, **177**, 2045-2051.
10. P. Metzger, K. A. Friedrich, G. Schiller and H. Müller-Steinhagen, *ECS Transactions*, 2007, **7**, 1841-1847.

- 1
2
3
4
5
6
7
8
9
10
11
12
13
14
15
16
17
18
19
20
21
22
23
24
25
26
27
28
29
30
31
32
33
34
35
36
37
38
39
40
41
42
43
44
45
46
47
48
49
50
51
52
53
54
55
56
57
58
59
60
11. M. A. Khaleel and J. R. Selman, in *High-temperature solid oxide fuel cells: Fundamentals, design and application*, eds. S. C. Singhal and K. Kendall, Elsevier Science, Oxford, 2003, pp. 291-331.
 12. S. B. Adler and W. G. Bessler, in *Handbook of Fuel Cells - Fundamentals, Technology and Applications, Vol. 5*, eds. W. Vielstich, H. Yokokawa and H. A. Gasteiger, John Wiley & Sons, Chichester, UK, 2009, pp. 441-462.
 13. W. G. Bessler, S. Gewies and M. Vogler, *Electrochim. Acta*, 2007, **53**, 1782-1800.
 14. W. G. Bessler and S. Gewies, *J. Electrochem. Soc.*, 2007, **154**, B548-B559.
 15. S. Gewies and W. G. Bessler, *J. Electrochem. Soc.*, 2008, **155**, B937-B952.
 16. M. Vogler, A. Bieberle-Hütter, L. J. Gauckler, J. Warnatz and W. G. Bessler, *J. Electrochem. Soc.*, 2009, **156**, B663-B672.
 17. W. H. Press, W. T. Vettering, S. A. Teukolsky and B. P. Flannery, *Numerical Recipes in C: The art of scientific computing*, Cambridge University Press, New York, 1992.
 18. A. V. Virkar, *J. Power Sources*, 2007, **172**, 713-724.
 19. F. S. Baumann, J. Fleig, H.-U. Habermeier and J. Maier, *Solid State Ionics*, 2006, **177**, 1071-1081.

Figure Captions

Fig. 1: Setup of measurement system for the characterization of planar segmented SOFCs with cathode segmentation for anode-supported cells.

Fig. 2: Model of the segmented SOFC. (a) Representation of segmentation by an electrical circuit. (b) Two-dimensional representation of one single gas channel including MEA and interconnect. (c) Surface electrochemistry of H₂ oxidation at the anode three-phase boundary.

Fig. 3: Comparison of experimental data under validation conditions (low fuel utilization) and 1D model calculations. (a) Variation of anode gas composition without N₂ at 800 °C with cathode at 100 % O₂; (b) Variation of anode gas dilution with 50 % H₂ and 50 % H₂O at 800 °C and cathode at 100 % O₂; (c) Variation of cathode gas composition at 800 °C with anode at 50 % H₂ and 50 % H₂O; (d) Variation of temperature with anode at 50 % H₂ and 50 % H₂O and cathode air.

Fig. 4: Measured two-dimensional distribution of power density over the 16 segments under operating conditions with high fuel utilization (counter-flow operation; anode: 33 % H₂, 1 % H₂O, 66 % N₂ in H₂, 1.1 m/s inflow velocity; cathode: air, 5.2 m/s inflow velocity; $T = 800$ °C) at a cell voltage of 0.59 V. The fuel inlet is at the left side, the air inlet at the right side.

Fig. 5: Experimental and simulated polarization behavior for the segmented cell using the 2D model under operating conditions with high fuel utilization (counter-flow operation; anode: 33 % H₂, 1 % H₂O, 66 % N₂ in H₂, 1.1 m/s inflow velocity; cathode: air, 5.2 m/s inflow velocity; $T = 800$ °C). (a) Global current-voltage curves, (b) Local segment voltage versus local segment current. The numbers indicate the segments, where segment 9 is the first in flow direction of the fuel gas.

Fig. 6: Distribution of local current density and gas-phase concentrations within channel and porous electrodes at anode and cathode side for the point of maximum power density P_{\max} (cf. Fig. 5). The numbers in the upper panel indicate the segments.

Fig. 7: Calculated contributions of polarization losses in segments 9 and 12 in dependence on cell voltage for the same operating conditions as shown in Fig. 5. The broken lines represent the condition of maximum power density (Fig. 6).

Tables

No.	Temperature [°C]	Anode			Cathode	
		% H ₂	% H ₂ O	% N ₂	% O ₂	% N ₂
1	800	50	50	0	21	79
2	800	97	3	0	100	0
3	800	90	10	0	100	0
4	800	50	50	0	100	0
5	800	25	25	50	100	0
6	800	5	5	90	100	0
7	800	50	50	0	5	95
8	750	50	50	0	21	79
9	700	50	50	0	21	79
10	800	33	1	66	21	79

Table 1: Experimental measurement conditions. Conditions 1-9 represent calibration conditions (low fuel utilization and specific N₂ dilution), condition 10 a realistic operating condition (high fuel utilization).

Model parameter	Value	Ref.
<i>Gas channel</i>		
Length	8.8 cm	Setup
Channel cross-sectional area	4 mm ²	Setup
Channel perimeter	4 mm	Setup
<i>Segmented cell</i>		
Number of segments in one channel	4	Setup
Segment area	2.2 cm x 2.2 cm	Setup
<i>Porous media</i> (mesh anode (ma), cermet anode (an), porous cathode (ca), mesh cathode (mc))		
Layer thickness: ma, an, ca, mc	450 μm, 540 μm, 55 μm, 490 μm	Setup
Porosity: ma, an, ca, mc	0.74, 0.32, 0.40 ^a , 0.82	Setup
Pore size: ma, an, ca, mc	100 μm, 0.7 μm, 0.5 μm ^a , 125 μm	Setup
Particle size: ca, mc	0.5 μm ^a , 40 μm	Setup
Tortuosity: ma, an, ca, mc	1.4 ^a , 2.9 ^b , 1.4 ^a , 1.4 ^a	
<i>Cermet anode</i>		
Active three-phase boundary length	4.5 · 10 ¹² m/m ³	Micro-structural model ¹⁵
Effective width electrolyte	0.43 μm	
Effective width electrode	0.31 μm	
Structural factor electrolyte conductivity	0.30	
<i>Electrolyte</i>		
Effective thickness	10 μm	Setup ¹⁵
Conductivity bulk 8YSZ: preexponential factor, activation energy	5.15 · 10 ⁷ SK/m, 84 kJ/mol	
<i>Additional resistances</i>		
Resistance of wires	1.4 Ωcm ^{2b}	Exp.
<i>Conditions</i>		
Temperature	700 - 800 °C	Exp.
Pressure	1013 hPa	Exp.

^a Estimated.

^b Fitted to the present experiments.

Table 2: Model parameters used for all calculations.

Anode Reaction	Preexponential factor	Activation energy	
<i>Charge transfer reaction (Fit):</i>			
$H_{Ni} + OH_{YSZ}^- \rightleftharpoons \square_{Ni} + H_2O_{YSZ} + e_{Ni}^-$	$1.63 \cdot 10^5 \text{ mol}/(\text{m s})^a$	235 kJ/mol^b	
<i>YSZ surface reactions:</i>			
$H_2O + \square_{YSZ} \rightleftharpoons H_2O_{YSZ}$	$6.6 \cdot 10^{11} \text{ mol}/(\text{cm}^3 \text{ s})$	0	
$H_2O_{YSZ} + O_{YSZ}^{2-} \rightleftharpoons 2 OH_{YSZ}^-$	$1.6 \cdot 10^{22} \text{ mol}/(\text{cm}^2 \text{ s})$	9.6 kJ/mol	
$O_{O_{YSZ}}^x + \square_{YSZ} \rightleftharpoons V_{O_{YSZ}}^{\bullet\bullet} + O_{YSZ}^{2-}$	$1.6 \cdot 10^{22} \text{ mol}/(\text{cm}^2 \text{ s})$	91 kJ/mol	
<i>Nickel surface reactions:</i>			
$H_2 + 2 \square_{Ni} \rightleftharpoons 2 H_{Ni}$	$9.8 \cdot 10^{17} \text{ mol}/(\text{cm}^5 \text{ s})$	0	
$H_2O + \square_{Ni} \rightleftharpoons H_2O_{Ni}$	$1.4 \cdot 10^{10} \text{ mol}/(\text{cm}^3 \text{ s})$	0	
$H_{Ni} + O_{Ni} \rightleftharpoons OH_{Ni} + \square_{Ni}$	$5.0 \cdot 10^{22} \text{ mol}/(\text{cm}^2 \text{ s})$	98 kJ/mol	
$H_2O_{Ni} + O_{Ni} \rightleftharpoons 2 OH_{Ni}$	$5.4 \cdot 10^{23} \text{ mol}/(\text{cm}^2 \text{ s})$	209 kJ/mol	
$H_{Ni} + OH_{Ni} \rightleftharpoons H_2O_{Ni} + \square_{Ni}$	$3.0 \cdot 10^{20} \text{ mol}/(\text{cm}^2 \text{ s})$	43 kJ/mol	
Cathode reaction	Exchange current density	Activation energy	Exponent a for p_{O_2}
$1/2 O_2 + V_{O_{YSZ}}^{\bullet\bullet} + 2 e^- \rightleftharpoons O_{O_{YSZ}}^x$	$4.4 \cdot 10^{10} \text{ A}/\text{m}^2^a$	125 kJ/mol^c	0.47^a

^a Fitted to the present experiments.

^b Fitted to experiments with symmetrical SOFC cermet anodes ¹⁵.

^c Activation energy from dense thin film electrodes ¹⁹.

Table 3: Elementary kinetic reaction mechanism for the anode and global kinetic reaction for the cathode. A single hydrogen spillover between Ni and YSZ surfaces is assumed as active charge-transfer reaction with a symmetry factor $\alpha = 0.5$. The surface site densities of Ni and YSZ are $6.1 \cdot 10^{-9}$ and $1.3 \cdot 10^{-9}$ mol/cm², respectively.

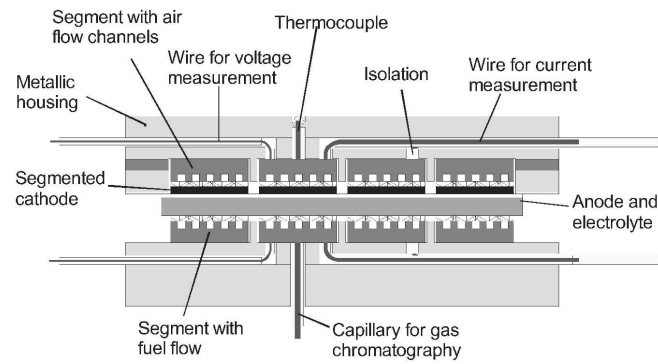


Fig. 1: Setup of measurement system for the characterization of planar segmented SOFCs with cathode segmentation for anode-supported cells.
150x210mm (600 x 600 DPI)

1
2
3
4
5
6
7
8
9
10
11
12
13
14
15
16
17
18
19
20
21
22
23
24
25
26
27
28
29
30
31
32
33
34
35
36
37
38
39
40
41
42
43
44
45
46
47
48
49
50
51
52
53
54
55
56
57
58
59
60

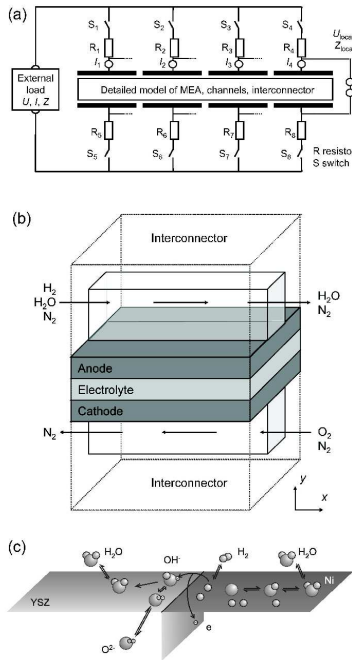


Fig. 2: Model of the segmented SOFC. (a) Representation of segmentation by an electrical circuit. (b) Two-dimensional representation of one single gas channel including MEA and interconnect. (c) Surface electrochemistry of H_2 oxidation at the anode three-phase boundary.

Fig. 2: Model of the segmented SOFC. (a) Representation of segmentation by an electrical circuit. (b) Two-dimensional representation of one single gas channel including MEA and interconnect. (c) Surface electrochemistry of H_2 oxidation at the anode three-phase boundary.
209x297mm (600 x 600 DPI)

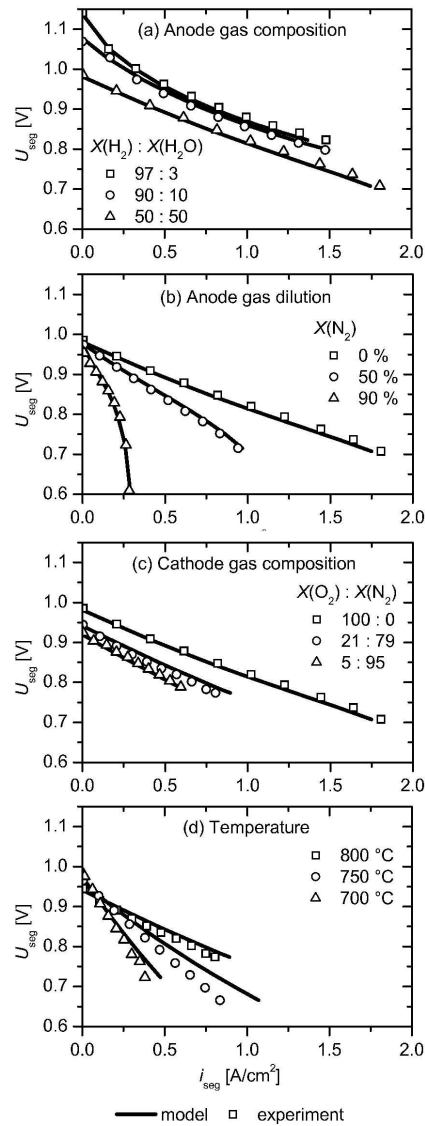


Fig. 3: Comparison of experimental data under validation conditions (low fuel utilization) and 1D model calculations. (a) Variation of anode gas composition without N₂ at 800 °C with cathode at 100 % O₂; (b) Variation of anode gas dilution with 50 % H₂ and 50 % H₂O at 800 °C and cathode at 100 % O₂; (c) Variation of cathode gas composition at 800 °C with anode at 50 % H₂ and 50 % H₂O; (d) Variation of temperature with anode at 50 % H₂ and 50 % H₂O and cathode air.
130x209mm (600 x 600 DPI)

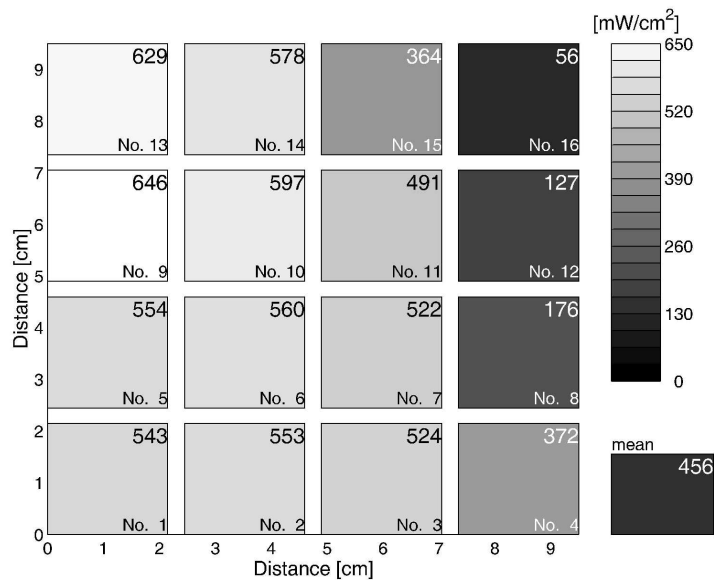


Fig. 4: Measured two-dimensional distribution of power density over the 16 segments under operating conditions with high fuel utilization (counter-flow operation; anode: 33 % H₂, 1 % H₂O, 66 % N₂ in H₂, 1.1 m/s inflow velocity; cathode: air, 5.2 m/s inflow velocity; T = 800 °C) at a cell voltage of 0.59 V. The fuel inlet is on the left side, the air inlet at the right side. 154x212mm (600 x 600 DPI)

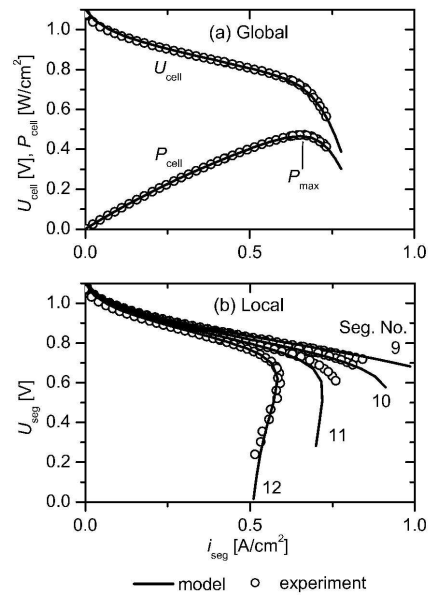


Fig. 5: Experimental and simulated polarization behavior for the segmented cell using the full 2D model under operating conditions with high fuel utilization (counter-flow operation; anode: 33 % H₂, 1 % H₂O, 66 % N₂ in H₂, 1.1 m/s inflow velocity; cathode: air, 5.2 m/s inflow velocity; T = 800 °C). (a) Global current-voltage curves. (b) Local segment voltage versus local segment current. The numbers indicate the segments, where segment 9 is the first in flow direction of the fuel gas.
116x210mm (600 x 600 DPI)

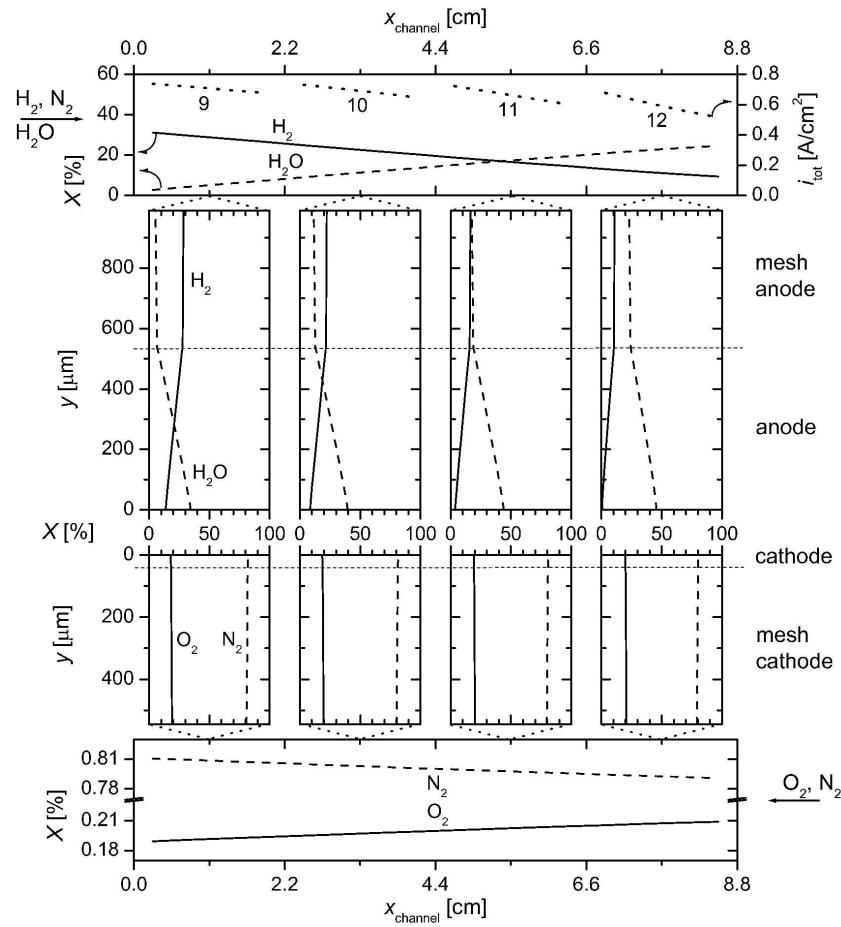


Fig. 6: Distribution of local current density and gas-phase concentrations within channel and porous electrodes on anode and cathode side for the point of maximum power density P_{max} (cf. Fig. 5).

The numbers in the upper panel indicate the segments.
169x206mm (600 x 600 DPI)

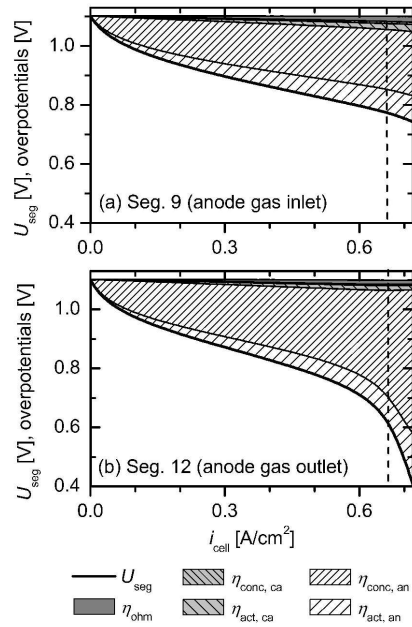


Fig. 7: Calculated contributions of polarization losses in segments 9 and 12 in dependence on cell voltage for the same operating conditions as shown in Fig. 5. The broken lines represent the condition of maximum power density (Fig. 6).
129x210mm (600 x 600 DPI)

Spatial Distribution of Electrochemical Performance in a Segmented SOFC: A Combined Modeling and Experimental Study

Wolfgang G. Bessler^{1,2*}, Stefan Gewies³, Caroline Willich¹, Günter Schiller¹, K. Andreas Friedrich¹

¹ Deutsches Zentrum für Luft- und Raumfahrt (DLR)
Institut für Technische Thermodynamik
Pfaffenwaldring 38-40
D-70569 Stuttgart / Germany

² Universität Stuttgart
Institut für Thermodynamik und Wärmetechnik
Pfaffenwaldring 6
D-70550 Stuttgart / Germany

³ Deutsches Zentrum für Luft- und Raumfahrt (DLR)
Institut für Kommunikation und Navigation
Kalkhorstweg 53
D-17235 Neustrelitz / Germany

* Corresponding author, email: wolfgang.bessler@dlr.de, phone: +49 711 6862603

Abstract

Spatially inhomogeneous distribution of current density and temperature in solid oxide fuel cells (SOFC) contributes to accelerated electrode degradation, thermomechanical stresses, and reduced efficiency. This paper presents a combined experimental and modeling study of the distributed electrochemical performance of a planar SOFC. Experimental data were obtained using a segmented cell setup that allows the measurement of local current-voltage characteristics, gas composition and temperature in 4×4 segments. Simulations were performed using a two-dimensional elementary kinetic model that represents the experimental setup in a detailed way. Excellent agreement between model and experiment was obtained for both global and local performance over all investigated operating conditions under varying H₂/H₂O/N₂ compositions at the anode, O₂/N₂ compositions at the cathode, temperature, and fuel utilization. A strong variation of the electrochemical performance along the flow path was observed when the cell was operated at high fuel utilization. The simulations predict a considerable gradient of gas-phase concentrations along the fuel channel and through the thickness of the porous anode, while the gradients are lower at the cathode side. The anode dominates polarization losses. The cell may operate locally in critical operating conditions (low H₂/H₂O ratios, low local segment voltage) without notably affecting globally observed electrochemical behavior.

Keywords: Solid oxide fuel cell (SOFC), Segmented cell, Experiment, Modeling, Simulation

Deleted: , Degradation

1 Introduction

High electrical efficiency and long-term durability are key requirements for a cost-competitive introduction of fuel cell technology. In order to achieve high efficiency, a high fuel utilization is required, that is, the complete fuel should be converted electrochemically in the fuel cell. In solid oxide fuel cells (SOFC), high fuel utilization results in strong concentration gradients at the anode, where the fuel (H₂, CO, CH₄) is successively diluted by reaction products (H₂O, CO₂). This, in turn, leads to an inhomogeneous distribution of electrochemical performance (local power density) and temperature. These inhomogeneities detrimentally affect both efficiency (through a large concentration polarization) and long-term stability (through thermomechanical stresses and local operating conditions that may induce degradation). In order to understand these effects, it is necessary to obtain detailed information about the spatial distribution of the electrical, chemical and thermal cell properties.

For polymer electrolyte fuel cells (PEFCs), segmented cell setups for the local measurement of current density have been developed and are widely used¹⁻⁷. In contrast to this, only few experiments for a spatially resolved characterization of SOFCs have been conducted so far, mainly because the high operating temperature (700-900 °C) represents a considerable challenge to the experimental setup. One of the first setups for the local characterization of segmented planar SOFC cells has been developed by Metzger et al.⁸⁻¹⁰.

Segmented-cell setups are typical model experiments in the sense that they allow a largely extended insight at the cost of modified geometries and/or materials in comparison to standard fuel cells. Results from segmented cells are therefore not expected to be quantitatively equivalent to those from standard stacks in terms of performance or temperature distribution. Having this difference in mind, the accessible information is highly valuable both for increasing the fundamental understanding and for optimizing cell and flow field design.

The use of mathematical modeling in combination with experimental investigations can significantly enhance the understanding of the spatially resolved electrochemical behavior of the cell. For example, today's experimental techniques do not allow the measurement of concentration and current distributions inside the porous electrodes. However, it is the electrochemically active zone inside the electrodes that governs electrochemical performance as well as degradation behavior. For this reason, modeling studies are increasingly used to aid understanding of the fuel cell processes and to optimize electrode and cell design^{11,12}. The combination of simulations with segmented-cell experiments is particularly useful because it allows reliable model validation including local behavior. Furthermore, the segmentation can easily be omitted and geometrical parameters be modified in the model, thus allowing to bridge the difference between the segmented cells and standard cells.

In this paper we present a combined modeling and experimental study of the spatial distribution of electrochemical performance in a planar SOFC. The experiments are based on the setup by Metzger et al.⁹. The simulations are conducted within a physically-based modeling framework developed by Bessler et al.¹³, which is extended in order to reflect the segmentation of the experimental setup. The following approach is used: (i) The model is validated using experimental polarization data under specifically designed calibration conditions; (ii) model predictions are compared with experimental data at realistic operating conditions; and (iii) the validated model is used for quantitative interpretation and prediction of the physical, electrochemical and fluid mechanical fuel cell properties.

2 Experimental Setup

The measurement setup for segmented cells has been described previously^{8,9}. It is shown schematically in Fig. 1a. Square-shaped anode-supported cells (100 cm² area, 540 μm Ni/YSZ cermet anode with a thin anode functional layer, 5 μm 8YSZ electrolyte, 3 μm YDC interlayer, 45 μm LSCF cathode divided into 16 segments with an active area of 4.84 cm² of each segment) were integrated in a metallic cell housing and sealed with glass seal (Fraunhofer Institute of Ceramic Technologies and Sintered Materials (IKTS), Dresden, Germany). The metallic housing is subdivided into 16 galvanically isolated segments with a total active area of 73.96 cm². The flow field is identical for fuel and air side; it consists of square-shaped channels (2 × 2 mm, 5 channels per segment row) that are supplied via inlet and outlet manifolds that are symmetrical to each other (ca. 4 cm³ per manifold).

In order to determine the temperature at each segment, thermocouples are introduced in the metallic segments. Additionally, capillary tubes that correspond to the cathodic segments are integrated at the anode side at 16 measuring points to take samples of the anode gas to be analyzed by gas chromatography. The setup allows for the integral and spatially resolved measurement of current density and voltage, the local and integral determination of impedance data, the local measurement of temperature and the spatially resolved analysis of the fuel gas concentrations along the flow path.

Experiments were conducted under a wide range of operating conditions as summarized in Table 1. Conditions for model calibration were defined that show a high sensitivity of simulated polarization curves on unknown model parameters. The calibration measurements were carried out under high gas flow rates (low fuel utilization) in order to avoid strong fuel depletion. Even for the highest fuel dilution (Table 1, condition 6), fuel utilization was < 26 %. Additional measurements were performed under realistic gas compositions at high fuel utilization (Table 1, condition 10).

3 Modeling and Simulation

3.1 Planar SOFC Modeling Framework

The framework for physically-based SOFC modeling and simulation has been presented previously¹³. The model layout is shown schematically in Fig. 2, and all model parameters are summarized in Table 2. A detailed 1D+1D elementary kinetic electrochemical model was applied that represents one single channel of the experimental setup (Fig. 2b). One-dimensional channel flow (*x* dimension) is described using the Navier-Stokes conservation equations (continuity, species, momentum), corresponding essentially to a plug-flow model with axial diffusion¹⁴. One-dimensional mass transport through the membrane-electrode assembly (MEA) (*y* dimension) is described by coupled Fickian/Knudsen diffusion and Darcy flow. Charge transport in the solid

Field Code Changed

Deleted: multi-scale

Field Code Changed

electrolyte and the electrolyte phase of the composite electrodes is described in two dimensions using Ohm's law.

The results shown in this paper are calculated under the assumption of isothermal conditions. This assumption is justified because measured temperature variations along the flow path are relatively low (26 K at a current density of 1.4 A/cm²) due to rapid heat losses via the metallic flow field and housing.

Anode electrochemistry is described using elementary kinetics for surface reactions on Ni and YSZ, and for charge transfer (hydrogen spillover) (Fig. 2c), as given in Table 3, and as validated by previous cermet anode and patterned anode studies^{15,16}. The electrochemical double layer is described as simple capacitor. Cathode electrochemistry is described using a modified Butler-Volmer equation,

$$i = i^0 p_{O_2}^a \exp(-E_{act}/RT) \cdot [\exp(0.5F\eta/RT) - \exp(-0.5F\eta/RT)] . \quad (1)$$

A definition of all symbols and their units is given in¹³. Current-voltage relationships are modeled by directly solving for the electric-potential distribution in the electrodes and electrolytes without using the Nernst equation. All models are implemented in the in-house numerical simulation software DENIS. For numerical simulation, the MEA was spatially discretized into 16 × 80 control volumes (x × y dimension). For identifying unknown model parameters, a Levenberg-Marquardt nonlinear least-squares fitting algorithm was used.

3.2 Segmentation

For the present study, the model described in Ref.¹³ was extended in order to include the cell segmentation of the experimental setup. The segmentation is represented by an electrical circuit model as shown in Fig. 2a. An arbitrary number and size of segments can be used at both anode and cathode. The segments are individually connected via switches S_i to outer power rails at anode and cathode side. These rails are assumed to be at constant potential ϕ given by the outer load. The connection wires are assumed to be resistors R_i, leading to a potential drop modeled via Ohm's law,

$$\Delta\phi = R i_{seg} , \quad (2)$$

where R is the cell-area-specific wire resistance and the potential drop $\Delta\phi$ depends on the segment current density i_{seg} . Along the length of each individual segment the potential and therefore the local segment voltage U_{local} are assumed constant. The simulation input is the voltage U of the external load. The model yields the total current I, the individual segment currents I_i, as well as local segment voltages U_{local} . The latter are determined experimentally via individual voltage probes (four-point measurements at each segment). The model can also be used to calculate global and local impedance Z and Z_{local}, respectively.

For the present simulations, four segments are used at both anode and cathode, and all switches S_i are closed, representing the experimental setup. The wire resistance R is determined via fitting to the experiments (cf. Table 2).

4 Results and Discussion

4.1 Calibration Measurements and Model Validation

There are a number of model parameters associated with electrochemistry and transport in the MEA that are specific for the investigated cells and cannot be obtained from literature. Some parameters can be reliably estimated (e.g., porosity from SEM micrographs). Other parameters, however, can only be obtained by fitting to experimental data. To this goal, the model was validated under specifically designed operating conditions (Table 1, conditions 1-9). Experimental polarization behavior was measured under low fuel utilization (< 15 % by using fast gas inflow velocities) in order to circumvent spatial gradients along the channel. Gas-phase anode and cathode inlet concentrations as well as temperature were varied over a range of conditions; these conditions were chosen in order to achieve sensitivity for the unknown parameters. Parameters were fitted using a one-dimensional model of the MEA only. Fitting results are included in Table 2 and Table 3.

In the present study, the following model parameters were fitted: (1) The preexponential factor of the elementary kinetic hydrogen spillover reaction at the anode (all other elementary kinetic parameters were used without modification from previous cermet anode studies¹⁵); (2) the exchange current density of the global kinetic charge-transfer reaction at the cathode; (3) the p_{O₂} exponent for cathode; (4) the tortuosity of the anode; (5) the ohmic resistance of the current collector wires. Given the high level of physicochemical detail of the present model, the number of free fit parameter has to be considered very low. It should be noted that the preexponential factor of the anodic charge-transfer reaction had to be modified by only 30 % in comparison to previous cermet anode studies¹⁵; this small modification can be interpreted as variations in material and/or microstructure and demonstrates how elementary kinetic approaches can reduce empiricism in fuel cell modeling.

Field Code Changed

Field Code Changed

Formatted: Superscript

Field Code Changed

Deleted: In the present study, the electrochemical performance of anode and cathode (preexponential factors, activation energies, p_{O₂} exponent for cathode), as well as porous anode tortuosity are used as free parameters. These parameters were fitted and the

Formatted: Superscript

Formatted: Superscript

1
2 | Simulated and experimental polarization curves for the validation conditions are shown in Fig. 3. There is
3 good quantitative agreement between model and experiment over the complete range of operating conditions
4 (anode H₂/H₂O ratio, anode gas dilution with N₂, cathode O₂/N₂ ratio, and temperature). Note that the physical
5 model uses only one single set of parameters for all conditions. A systematic deviation between model and
6 experiment occurs during temperature variation. We believe that this is due to an onset of cell degradation,
7 lowering the experimentally observed performance relative to the model predictions. Degradation effects are not
8 included in the model.

Deleted: ¶

9 4.2 Measurement and Simulation Under High Fuel Utilization

10 The segmented cell was operated under a condition with high fuel utilization (Table 1, condition 10). The
11 anode was fed with 33% H₂, 1% H₂O and 66% N₂. This condition was chosen in order to simulate nitrogen-rich
12 reformate gas. The cathode was fed with air in counter-flow operation.

13 The measured two-dimensional distribution of power density in the 16 segments is shown in Fig. 4 for an
14 average power density of 460 mW/cm². The fuel utilization at this condition is 80%. The cell performance is
15 strongly inhomogeneous, with the power density systematically decreasing from fuel inlet (left side of Fig. 4)
16 to fuel outlet (right side of Fig. 4). It will be shown below that this decrease is due to fuel depletion along the
17 flow path. Moreover, there is a notable difference for the four segment rows (upper row to lower row in Fig. 4). This
18 difference may be due to sealing issues or inhomogeneous gas supply to the gas channels. Further segment-to-
19 segment scattering is likely due to a variation in contact resistance, which may also lead to systematic row-to-
20 row variations when the contact pressure is inhomogeneous. For comparison with the model (which represents
21 the behavior along one single channel), the row with segments 9-12 was chosen.

22 Experimental and simulated global and local current-voltage characteristics for segments 9-12 are shown in
23 Fig. 5. Simulations were performed using the 2D model (i.e., along one representative channel and through the
24 thickness of the MEA, cf. Fig. 2). The global IV-curve (Fig. 5a) shows a typical shape with a parabolic behavior
25 at low currents, linear behavior at intermediate currents, and a limiting current density of ~0.8 A/cm² at high
26 currents. The maximum power density ($P_{\max} = 470 \text{ mW/cm}^2$) is observed at a cell voltage of 0.70 V. Local IV-
27 curves for segments 9-12 are represented by plotting local segment voltage versus local segment current (Fig.
28 5b). The local behavior shows a considerable variation of current density for different cell segments. At high
29 polarization, segments 11 and 12 that are located close to the fuel outlet show a particularly interesting behavior:
30 the current decreases while at the same time the segment voltage strongly decreases. This "inverse" behavior is
31 due to strong fuel depletion (see next section). At the same time, the current density of segment 9 that is located
32 at the fuel inlet continues to increase.

33 There is excellent quantitative agreement between model and experiment for both the local and the global
34 behavior. Note that no additional parameter adjustment was performed after model calibration (Section 4.1). This
35 finding also underlines the validity of the choice of calibration conditions.

36 4.3 Distribution of Gas-Phase Concentrations

37 Fig. 6 shows the simulated spatially resolved distribution of gas-phase concentrations in the channels as well
38 as in the porous electrodes and current collector meshes for the condition of maximum power density (P_{\max} in
39 Fig. 5a). There are considerable concentration gradients throughout the complete system. In particular, the
40 relatively thick porous anode in this anode-supported cell is responsible for strong H₂ depletion through the
41 anode thickness. This is the case, in particular, for segments 11 and 12. Here, H₂ concentration tends towards
42 zero at the porous electrode/solid electrolyte interface. This is the reason for the strong decrease in segment
43 voltage observed in the local IV-curves (Fig. 5b).

44 The upper panel of Fig. 6 also shows the local current density along the flow path. The step-like behavior of
45 the four segments is due to the contribution of the resistance of current collector wires (cf. Fig. 2a): The potential
46 drop over the wire for the individual segments decreases as the overall segment current decreases along the fuel
47 flow path (left to right in Fig. 6). This leads to an increase in integral segment current, causing a step from the
48 end of one segment to the beginning of the next segment. Note that the segment voltage is measured and
49 simulated directly at the segment (U_{local} in Fig. 2a), therefore including the wire resistance. The current density
50 distribution along the length of each segment is inhomogeneous. The integral current density over one segment is
51 shown in Fig. 5b.

52 The condition of strong fuel depletion observed inside the porous anode may be highly critical concerning
53 cell degradation. In particular, low H₂/H₂O ratios may lead to nickel oxidation at the anode, and low local
54 segment voltages may lead to cathode degradation¹⁸. Note that the critical behavior observed here in particular
55 at segment 12 is not obvious from the global IV-behavior. Thus, a cell may be locally in a critical operating
56 condition while global characteristics are well within apparent stability limits (e.g., sufficiently high global cell
57 voltage). Post-test analysis and interpretation with a focus on degradation is subject of ongoing studies.

Field Code Changed

Deleted: 17

58 4.4 Distribution of Polarization Losses

The knowledge of the physical origin of polarization losses is a requirement for an optimization of cell design and operating conditions. The validated model offers the possibility to quantify the spatially varying polarization losses. Results for segments 9 and 12 are shown in Fig. 7 for the same operating conditions as shown in Fig. 5. The total polarization losses are separated into contributions from Ohmic resistance of the electrolyte η_{ohm} , concentration polarization η_{conc} at both anode and cathode, and activation polarization η_{act} at both anode and cathode.

For both segments, concentration polarization at the anode is the dominant loss process. This finding is consistent with the observation of strong H_2 depletion along the channel and through the anode thickness. The second largest contribution is anode activation. Polarization due to the electrolyte and cathode activation and concentration losses are low and do not significantly affect the cell performance. With increasing current density, all losses increase up to the point of maximum power density. Beyond that point, Ohmic and activation losses decrease in segment 12 due to the decreasing local current density in these segments (cf. Fig. 5b).

The analysis shows that the parabolic behavior at low current density that is observed in the global IV-curve (Fig. 5a) is due to anode concentration polarization and not, as commonly assumed, due to activation polarization. This has been pointed out before¹⁴. In this respect, SOFCs behave differently from PEFCs where low-current parabolic behavior is indeed due to activation losses.

5 Conclusions

A combined experimental and modeling study of the spatial distribution of the electrochemical performance in a planar SOFC was performed. Experimental data were obtained using a specifically designed segmented cell setup that allows for the measurement of local current-voltage characteristics, gas composition and temperature. Simulations were performed using a two-dimensional elementary kinetic model that represents the experimental setup in a highly detailed way.

Model parameters were identified by comparing simulations with validation experiments under low fuel utilization. Experiments and simulations under high fuel utilization showed strong gradients of gas concentrations and current density along the flow path and throughout the thickness of the membrane-electrode assembly. Over the complete range of operating conditions, excellent quantitative agreement between model and experiment for both global and local behavior was observed. The relatively thick porous anode and high fuel utilization causes particularly strong concentration variations at the anode, while the gradients are lower at the cathode side. The combined modeling and experimental study allows for the reliable quantification of the contribution of various polarization losses. It was shown that concentration polarization at the anode is the dominant loss process, followed by anode activation polarization. The anode was therefore identified as the critical component in this cell type.

An important conclusion is that the cell may operate locally in critical operating conditions (low $\text{H}_2/\text{H}_2\text{O}$ ratios, low local segment voltage) without notably affecting global electrochemical behavior. These conditions are likely to detrimentally affect cell durability. Based on a combination of experiment and modeling, the present study allows for identifying such conditions and for assessing optimized cell design and operation strategies.

Acknowledgements

Funding was provided by the Umweltministerium Baden-Württemberg, Germany, through the programme "Herausforderung Brennstoffzelle" (ZO4 BW26037 and ZO4 BW26038).

References

1. M. Noponen, T. Tennola, M. Mikkola, T. Hottinen and P. Lund, *J. Power Sources*, 2002, **106**, 304-312.
2. D. J. L. Brett, S. Atkins, N. P. Brandon, V. Vesovic, N. Vasileiadis and A. R. Kucernak, *Electrochemistry Communications*, 2001, **3**, 628-632.
3. N. Rajalakshmi, M. Raja and K. S. Dhathathreyan, *J. Power Sources*, 2002, **112**, 331-336.
4. G. Bender, M. S. Wilson and T. A. Zawodzinski, *J. Power Sources*, 2003, **123**, 163-171.
5. S. Schönbauer and H. Sander, in *3rd European PEFC Forum*, Lucerne, Switzerland, 2005, p. B056.
6. I. A. Schneider, S. A. Freunberger, D. Kramer, A. Wokaun and G. G. Scherer, *J. Electrochem. Soc.*, 2007, **154**, B383-B388.
7. M. Schulze, E. Gülzow, S. Schönbauer, T. Knöri and R. Reissner, *J. Power Sources*, 2007, **173**, 19-27.
8. P. Metzger, G. Schiller and A. O. Störmer, in *6th European Solid Oxide Fuel Cell Forum*, Lucerne, Switzerland, 2004, pp. 989-999.
9. P. Metzger, K.-A. Friedrich, H. Müller-Steinhagen and G. Schiller, *Solid State Ionics*, 2006, **177**, 2045-2051.
10. P. Metzger, K. A. Friedrich, G. Schiller and H. Müller-Steinhagen, *ECS Transactions*, 2007, **7**, 1841-1847.

Field Code Changed

Formatted: Font: Italic

Formatted: Font: Bold

Formatted: Font: German (Germany)

Formatted: Font: Italic, German (Germany)

Formatted: Font: German (Germany)

Formatted: Font: Italic, German (Germany)

Formatted: Font: German (Germany)

Formatted: Font: Bold, German (Germany)

Formatted: Font: German (Germany)

Formatted: Font: Italic, German (Germany)

Formatted: Font: German (Germany)

Formatted: Font: Bold, German (Germany)

Formatted: Font: German (Germany)

Formatted: Font: Italic, German (Germany)

Formatted: Font: German (Germany)

Formatted: Font: Italic, German (Germany)

Formatted: Font: German (Germany)

Formatted: Font: Bold, German (Germany)

Formatted: Font: German (Germany)

Formatted: Font: Italic, German (Germany)

Formatted: Font: German (Germany)

Formatted: Font: Bold, German (Germany)

Formatted: Font: German (Germany)

11. M. A. Khaleel and J. R. Selman, in *High-temperature solid oxide fuel cells: Fundamentals, design and application*, eds. S. C. Singhal and K. Kendall, Elsevier Science, Oxford, 2003, pp. 291-331.
12. S. B. Adler and W. G. Bessler, in *Handbook of Fuel Cells - Fundamentals, Technology and Applications*, Vol. 5, eds. W. Vielstich, H. Yokokawa and H. A. Gasteiger, John Wiley & Sons, Chichester, UK, 2009, pp. 441-462.
13. W. G. Bessler, S. Gewies and M. Vogler, *Electrochim. Acta*, 2007, **53**, 1782-1800.
14. W. G. Bessler and S. Gewies, *J. Electrochem. Soc.*, 2007, **154**, B548-B559.
15. S. Gewies and W. G. Bessler, *J. Electrochem. Soc.*, 2008, **155**, B937-B952.
16. M. Vogler, A. Bieberle-Hütter, L. J. Gauckler, J. Warnatz and W. G. Bessler, *J. Electrochem. Soc.*, 2009, **156**, B663-B672.
17. W. H. Press, W. T. Vetterling, S. A. Teukolsky and B. P. Flannery, *Numerical Recipes in C: The art of scientific computing*, Cambridge University Press, New York, 1992.
18. A. V. Virkar, *J. Power Sources*, 2007, **172**, 713-724.
19. F. S. Baumann, J. Fleig, H.-U. Habermeier and J. Maier, *Solid State Ionics*, 2006, **177**, 1071-1081.

Figure Captions

Fig. 1: Setup of measurement system for the characterization of planar segmented SOFCs with cathode segmentation for anode-supported cells.

Fig. 2: Model of the segmented SOFC. (a) Representation of segmentation by an electrical circuit. (b) Two-dimensional representation of one single gas channel including MEA and interconnect. (c) Surface electrochemistry of H₂ oxidation at the anode three-phase boundary.

Fig. 3: Comparison of experimental data under validation conditions (low fuel utilization) and 1D model calculations. (a) Variation of anode gas composition without N₂ at 800 °C with cathode at 100 % O₂; (b) Variation of anode gas dilution with 50 % H₂ and 50 % H₂O at 800 °C and cathode at 100 % O₂; (c) Variation of cathode gas composition at 800 °C with anode at 50 % H₂ and 50 % H₂O; (d) Variation of temperature with anode at 50 % H₂ and 50 % H₂O and cathode air.

Fig. 4: Measured two-dimensional distribution of power density over the 16 segments under operating conditions with high fuel utilization (counter-flow operation; anode: 33 % H₂, 1 % H₂O, 66 % N₂ in H₂, 1.1 m/s inflow velocity; cathode: air, 5.2 m/s inflow velocity; T = 800 °C) at a cell voltage of 0.59 V. The fuel inlet is at the left side, the air inlet at the right side.

Fig. 5: Experimental and simulated polarization behavior for the segmented cell using the 2D model under operating conditions with high fuel utilization (counter-flow operation; anode: 33 % H₂, 1 % H₂O, 66 % N₂ in H₂, 1.1 m/s inflow velocity; cathode: air, 5.2 m/s inflow velocity; T = 800 °C). (a) Global current-voltage curves, (b) Local segment voltage versus local segment current. The numbers indicate the segments, where segment 9 is the first in flow direction of the fuel gas.

Fig. 6: Distribution of local current density and gas-phase concentrations within channel and porous electrodes at anode and cathode side for the point of maximum power density P_{\max} (cf. Fig. 5). The numbers in the upper panel indicate the segments.

Fig. 7: Calculated contributions of polarization losses in segments 9 and 12 in dependence on cell voltage for the same operating conditions as shown in Fig. 5. The broken lines represent the condition of maximum power density (Fig. 6).

Formatted: Font: Italic

Formatted: Font: Italic

Formatted: Font: Italic

Formatted: Font: Bold

Formatted: Font: Italic

Formatted: Font: Bold

Formatted: Font: Italic

Formatted: Font: Italic, German (Germany)

Formatted: German (Germany)

Formatted: Font: Bold, German (Germany)

Formatted: German (Germany)

Formatted: Font: Italic, German (Germany)

Formatted: Font: Italic

Formatted: Font: Bold

Formatted: Font: Italic

Formatted: Font: Italic

Formatted: Font: Bold

Formatted: German (Germany)

Formatted: Font: Italic, German (Germany)

Formatted: German (Germany)

Formatted: Font: Bold, German (Germany)

Formatted: German (Germany)

Formatted: Indent: Left: 0 pt, First line: 0 pt

Deleted: 1. . M. Noponen, T. Tennola, M. Mikkola, T. Hottinen and P. Lund, *J. Power Sources*, 2002, **106**, 304-312.¶
 2. . D. J. L. Brett, S. Atkins, N. P. Brandon, V. Vesovic, N. Vasileiadis and A. R. Kucernak, *Electrochemistry Communications*, 2001, **3**, 628-632.¶
 3. . N. Rajalakshmi, M. Raja and K. S. Dhathathreyan, *J. Power Sources*, 2002, **112**, 331-336.¶
 4. . G. Bender, M. S. Wilson and T. A. Zawodzinski, *J. Power Sources*, 2003, **123**, 163-171.¶
 5. . S. Schönbauer and H. Sander, in *3rd European PEFC Forum*, Lucerne, Switzerland, 2005, p. B056.¶
 6. . I. A. Schneider, S. A. Freunberger, D. Kramer, A. Wokaun and G. G. Scherer, *J. Electrochem. Soc.*, 2007, **154**, B383-B388.¶
 7. . M. Schulze, E. Gülzow, S. Schönbauer, T. Knöri and R. Reissner, *J. Power Sources*, 2007, **173**, 19-27.¶
 8. . P. Metzger, G. Schiller and A. O. Störmer, in *6th European Solid Oxide Fuel Cell Forum*, Lucerne, Switzerland, 2004, pp. 989-999.¶
 9. . P. Metzger, K.-A. Friedrich, H. Müller-Steinhagen and G. Schiller [1]

Formatted: German (Germany)

Formatted: German (Germany)

Tables

No.	Temperature [°C]	Anode			Cathode	
		% H ₂	% H ₂ O	% N ₂	% O ₂	% N ₂
1	800	50	50	0	21	79
2	800	97	3	0	100	0
3	800	90	10	0	100	0
4	800	50	50	0	100	0
5	800	25	25	50	100	0
6	800	5	5	90	100	0
7	800	50	50	0	5	95
8	750	50	50	0	21	79
9	700	50	50	0	21	79
10	800	33	1	66	21	79

Table 1: Experimental measurement conditions. Conditions 1-9 represent calibration conditions (low fuel utilization and specific N₂ dilution), condition 10 a realistic operating condition (high fuel utilization).

Model parameter	Value	Ref.
<i>Gas channel</i>		
Length	8.8 cm	Setup
Channel cross-sectional area	4 mm ²	Setup
Channel perimeter	4 mm	Setup
<i>Segmented cell</i>		
Number of segments in one channel	4	Setup
Segment area	2.2 cm x 2.2 cm	Setup
<i>Porous media</i> (mesh anode (ma), cermet anode (an), porous cathode (ca), mesh cathode (mc))		
Layer thickness: ma, an, ca, mc	450 μm, 540 μm, 55 μm, 490 μm	Setup
Porosity: ma, an, ca, mc	0.74, 0.32, 0.40 ^a , 0.82	Setup
Pore size: ma, an, ca, mc	100 μm, 0.7 μm, 0.5 μm ^a , 125 μm	Setup
Particle size: ca, mc	0.5 μm ^a , 40 μm	Setup
Tortuosity: ma, an, ca, mc	1.4 ^a , 2.9 ^b , 1.4 ^a , 1.4 ^a	
<i>Cermet anode</i>		
Active three-phase boundary length	4.5 · 10 ¹² m/m ³	Micro-structural model ¹⁵
Effective width electrolyte	0.43 μm	
Effective width electrode	0.31 μm	
Structural factor electrolyte conductivity	0.30	
<i>Electrolyte</i>		
Effective thickness	10 μm	Setup ¹⁵
Conductivity bulk 8YSZ: preexponential factor, activation energy	5.15 · 10 ⁷ SK/m, 84 kJ/mol	Field Code Changed
<i>Additional resistances</i>		
Resistance of wires	1.4 Ωcm ^{2b}	Exp.
<i>Conditions</i>		
Temperature	700 - 800 °C	Exp.
Pressure	1013 hPa	Exp.

^a Estimated.

^b Fitted to the present experiments.

Table 2: Model parameters used for all calculations.

Anode Reaction	Preexponential factor	Activation energy	
<i>Charge transfer reaction (Fit):</i>			
$\text{H}_{\text{Ni}} + \text{OH}^-_{\text{YSZ}} \rightleftharpoons \square_{\text{Ni}} + \text{H}_2\text{O}_{\text{YSZ}} + \text{e}^-_{\text{Ni}}$	$1.63 \cdot 10^5 \text{ mol}/(\text{m s})^a$	235 kJ/mol^b	
<i>YSZ surface reactions:</i>			
$\text{H}_2\text{O} + \square_{\text{YSZ}} \rightleftharpoons \text{H}_2\text{O}_{\text{YSZ}}$	$6.6 \cdot 10^{11} \text{ mol}/(\text{cm}^3 \text{ s})$	0	
$\text{H}_2\text{O}_{\text{YSZ}} + \text{O}^{2-}_{\text{YSZ}} \rightleftharpoons 2 \text{OH}^-_{\text{YSZ}}$	$1.6 \cdot 10^{22} \text{ mol}/(\text{cm}^2 \text{ s})$	9.6 kJ/mol	
$\text{O}^x_{\text{YSZ}} + \square_{\text{YSZ}} \rightleftharpoons \text{V}^{\bullet\bullet}_{\text{O}_{\text{YSZ}}} + \text{O}^{2-}_{\text{YSZ}}$	$1.6 \cdot 10^{22} \text{ mol}/(\text{cm}^2 \text{ s})$	91 kJ/mol	
<i>Nickel surface reactions:</i>			
$\text{H}_2 + 2 \square_{\text{Ni}} \rightleftharpoons 2 \text{H}_{\text{Ni}}$	$9.8 \cdot 10^{17} \text{ mol}/(\text{cm}^3 \text{ s})$	0	
$\text{H}_2\text{O} + \square_{\text{Ni}} \rightleftharpoons \text{H}_2\text{O}_{\text{Ni}}$	$1.4 \cdot 10^{10} \text{ mol}/(\text{cm}^3 \text{ s})$	0	
$\text{H}_{\text{Ni}} + \text{O}_{\text{Ni}} \rightleftharpoons \text{OH}_{\text{Ni}} + \square_{\text{Ni}}$	$5.0 \cdot 10^{22} \text{ mol}/(\text{cm}^2 \text{ s})$	98 kJ/mol	
$\text{H}_2\text{O}_{\text{Ni}} + \text{O}_{\text{Ni}} \rightleftharpoons 2 \text{OH}_{\text{Ni}}$	$5.4 \cdot 10^{23} \text{ mol}/(\text{cm}^2 \text{ s})$	209 kJ/mol	
$\text{H}_{\text{Ni}} + \text{OH}_{\text{Ni}} \rightleftharpoons \text{H}_2\text{O}_{\text{Ni}} + \square_{\text{Ni}}$	$3.0 \cdot 10^{20} \text{ mol}/(\text{cm}^2 \text{ s})$	43 kJ/mol	
<i>Cathode reaction</i>			
	Exchange current density	Activation energy	Exponent a for p_{O_2}
$1/2 \text{O}_2 + \text{V}^{\bullet\bullet}_{\text{O}_{\text{YSZ}}} + 2 \text{e}^- \rightleftharpoons \text{O}^x_{\text{O}_{\text{YSZ}}}$	$4.4 \cdot 10^{10} \text{ A}/\text{m}^2^a$	125 kJ/mol^c	0.47^a

^a Fitted to the present experiments.

^b Fitted to experiments with symmetrical SOFC cermet anodes¹⁵.

^c Activation energy from dense thin film electrodes¹⁹.

Field Code Changed

Field Code Changed

Deleted: ¹⁸

Table 3: Elementary kinetic reaction mechanism for the anode and global kinetic reaction for the cathode. A single hydrogen spillover between Ni and YSZ surfaces is assumed as active charge-transfer reaction with a symmetry factor $\alpha = 0.5$. The surface site densities of Ni and YSZ are $6.1 \cdot 10^{-9}$ and $1.3 \cdot 10^{-9} \text{ mol}/\text{cm}^2$, respectively.

Page 6: [1] Deleted

Wolfgang G. Bessler

12/8/2009 8:30:00 AM

1. M. Noponen, T. Tennola, M. Mikkola, T. Hottinen and P. Lund, *J. Power Sources*, 2002, **106**, 304-312.
2. D. J. L. Brett, S. Atkins, N. P. Brandon, V. Vesovic, N. Vasileiadis and A. R. Kucernak, *Electrochemistry Communications*, 2001, **3**, 628-632.
3. N. Rajalakshmi, M. Raja and K. S. Dhathathreyan, *J. Power Sources*, 2002, **112**, 331-336.
4. G. Bender, M. S. Wilson and T. A. Zawodzinski, *J. Power Sources*, 2003, **123**, 163-171.
5. S. Schönbauer and H. Sander, in *3rd European PEFC Forum*, Lucerne, Switzerland, 2005, p. B056.
6. I. A. Schneider, S. A. Freunberger, D. Kramer, A. Wokaun and G. G. Scherer, *J. Electrochem. Soc.*, 2007, **154**, B383-B388.
7. M. Schulze, E. Gülzow, S. Schönbauer, T. Knöri and R. Reissner, *J. Power Sources*, 2007, **173**, 19-27.
8. P. Metzger, G. Schiller and A. O. Störmer, in *6th European Solid Oxide Fuel Cell Forum*, Lucerne, Switzerland, 2004, pp. 989-999.
9. P. Metzger, K.-A. Friedrich, H. Müller-Steinhagen and G. Schiller, *Solid State Ionics*, 2006, **177**, 2045-2051.
10. P. Metzger, K. A. Friedrich, G. Schiller and H. Müller-Steinhagen, *ECS Transactions*, 2007, **7**, 1841-1847.
11. M. A. Khaleel and J. R. Selmán, in *High-temperature solid oxide fuel cells: Fundamentals, design and application*, eds. S. C. Singhal and K. Kendall, Elsevier Science, Oxford, 2003, pp. 291-331.
12. S. B. Adler and W. G. Bessler, in *Handbook of Fuel Cells - Fundamentals, Technology and Applications, Vol. 5*, eds. W. Vielstich, H. Yokokawa and H. A. Gasteiger, John Wiley & Sons, Chichester, UK, 2009, pp. 441-462.
13. W. G. Bessler, S. Gewies and M. Vogler, *Electrochim. Acta*, 2007, **53**, 1782-1800.
14. W. G. Bessler and S. Gewies, *J. Electrochem. Soc.*, 2007, **154**, B548-B559.
15. S. Gewies and W. G. Bessler, *J. Electrochem. Soc.*, 2008, **155**, B937-B952.
16. M. Vogler, A. Bieberle-Hütter, L. J. Gauckler, J. Warnatz and W. G. Bessler, *J. Electrochem. Soc.*, 2009, **156**, B663-B672.
17. A. V. Virkar, *J. Power Sources*, 2007, **172**, 713-724.
18. F. S. Baumann, J. Fleig, H.-U. Habermeier and J. Maier, *Solid State Ionics*, 2006, **177**, 1071-1081.